Nanoscale

Accepted Manuscript

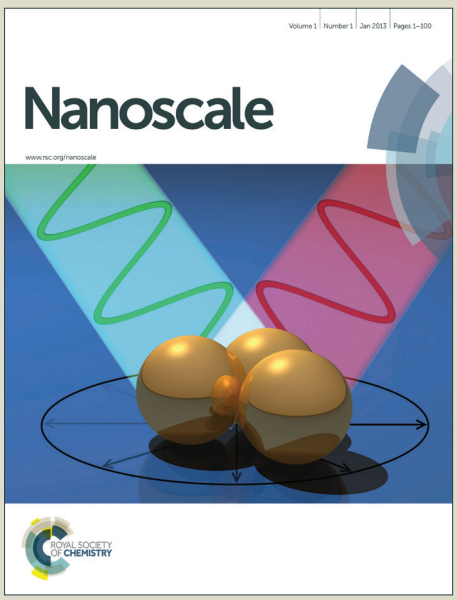

This is an *Accepted Manuscript*, which has been through the Royal Society of Chemistry peer review process and has been accepted for publication.

Accepted Manuscripts are published online shortly after acceptance, before technical editing, formatting and proof reading. Using this free service, authors can make their results available to the community, in citable form, before we publish the edited article. We will replace this *Accepted Manuscript* with the edited and formatted *Advance Article* as soon as it is available.

You can find more information about *Accepted Manuscripts* in the Information for Authors.

Please note that technical editing may introduce minor changes to the text and/or graphics, which may alter content. The journal's standard Terms & Conditions and the Ethical guidelines still apply. In no event shall the Royal Society of Chemistry be held responsible for any errors or omissions in this *Accepted Manuscript* or any consequences arising from the use of any information it contains.

ROYAL SOCIETY OF CHEMISTRY

www.rsc.org/nanoscale

Bottom-Up Synthesis of Nitrogen-Doped Graphene Sheets for Ultrafast Lithium Storage

Lei-Lei Tian[1,2], Xian-Yong Wei[1*], Quan-Chao Zhuang[2*], Chen-Hui Jiang[2], Chao Wu[1,2], Guang-Yao Ma[2], Xing Zhao[1,2], Zhi-Min Zong[1], Shi-Gang Sun[3]

[1] School of Chemical Engineering and Technology, China University of Mining & Technology, Xuzhou 221116, China; [2] School of Materials Science and Engineering, China University of Mining & Technology, Xuzhou 221116, China; [3] State Key Laboratory of Physical Chemistry of Solid Surfaces, Department of Chemistry, College of Chemistry and Chemical Engineering, Xiamen University, Xiamen 361005, China

Abstract: A facile bottom-up strategy was developed to fabricate nitrogen-doped graphene sheets (NGS) from glucose using a sacrificial template synthesis method. Three main types of nitrogen dopants (pyridinic, pyrrolic and graphitic nitrogens) were introduced into the graphene lattice, and inimitable microporous structure of NGS with a high specific surface area of 504 $m^2 g^{-1}$ was obtained. Particularly, with a hybrid feature of lithium ion batteries and faradic capacitor at a low rate and a faradic capacitor feature at a high rate, the NGS presents a superior lithium storage performance. During electrochemical cycling, the NGS electrode afforded enhanced reversible capacity of 832.4 mAh g^{-1} at 100 mA g^{-1} and excellent cycling stability of 750.7 mAh g^{-1} after 108 discharge/charge cycles. Furthermore, astonishing rate

*Corresponding author. Tel: +86 516 83591877 Fax: +86 516 83591870.
E-mail address: wei_xianyong@163.com (X.Y.W.) ; zhuangquanchao@126.com (Q.C.Z.)

Nanoscale Accepted Manuscript

capability of 333 mAh g^{-1} at 10000 mA g^{-1} and high rate cycle performance of 280.6 mAh g^{-1} even after 1200 cycles were also achieved, highlighting the significance of nitrogen doping on the maximum utilization of graphene-based materials for advanced lithium storage.

Keywords: graphene, nitrogen doping, template synthesis, rate performance, lithium ion batteries

Nanoscale Accepted Manuscript

1 Introduction

To design advanced energy storage devices, electrode materials with both high energy and high power density are urgently and essentially needed. Hence it is required to incorporate the features of supercapacitors with high rate performance and rechargeable batteries with high energy densities into a single unit.[1] Graphene, defined as a monolayer of sp^2-hybridized carbon atoms arranged in a honeycomb lattice, has become one of the most exciting materials in recent years.[2,3] By virtue of its extraordinary physicochemical properties, including large surface area, high conductivity, structural flexibility and chemical stability, graphene has been intensively explored as electrode materials and/or substrate of hybrid materials for high performance lithium ion batteries (LIBs).[4-14] It is commonly estimated that graphene might be more suitable for reversible lithium storage than commercial bulk graphite, because the graphene sheets could double the sorption capacity by bounding lithium ion on both sides of the graphene plane and by shortening the lithium diffusion distance.[4,5,15-21] However, it is recently concluded that the lithium coverage on the surface of single layer graphene is actually smaller, because of the lower binding energies of lithium to carbon and the strong Coulombic repulsion of the lithium atoms on the opposite sides of the graphene as well as the small charge transfer between lithium and graphene.[17,22,23] Moreover, the Li^+ diffusion parallel to the graphene planes is seriously hindered by the higher diffusion barrier resulting from the accumulated Li^+ in large area multilayer graphenes (MLG).[24]

Fortunately, heteroatomic dopants could substantially increase the lithium storage

Nanoscale Accepted Manuscript

performances of the carbon materials.[25] Nitrogen is one of the most attractive modification dopants because its electronegativity is higher than that of carbon and its atomic diameter is close to that of carbon.[26-34] The enhanced binding interactions between the nitrogen dopants and lithium might sharply increase the lithium coverage of graphene layer.[26,35] In addition, appropriate incorporation of nitrogen in graphitic networks could boost the electronic conductivity and reversibly cycle lithium ions.[35-37] Furthermore, alongside of the nitrogen dopants, considerable defects were also introduced, which could lower the diffusion barriers and thus facilitate the Li^+ diffusion through/cross the graphene layers.[24] Nitrogen-doped graphene has been heretheto fabricated through two main routes[38]: one is direct synthesis, including chemical vapor deposition (CVD)[28-30] and solvothermal[34] etc., the other is post-treatment doping, such as fumigation in NH_3,[25,31-33,39] plasma treatment[40,41] and hydrazine hydrate[42,43] etc. However, most of these methods are complicated and cannot achieve homogeneous nitrogen doping with high nitrogen content.

Herein, we report a facile bottom-up strategy to fabricate nitrogen-doped graphene sheets (NGS) as an ultrafast lithium storage material for advanced LIBs. During the sacrificial template synthesis process, the mixture of glucose and dicyandiamide was first thermally polymerized to create layered stacks of graphic carbon nitride (GCN, g-C_3N_4) template, and aromatic carbon intermediates were enclosed within the interlayer gaps of GCN simultaneously. NGS with microporous nanoarchitecture was finally achieved when the GCN template undergoes thermolysis. The unique

Nanoscale Accepted Manuscript

microporous nanoarchitecture could efficiently increase the interfacial interaction and improve the Li^+ diffusion. During the electrochemical cycles, the NGS could store lithium with hybrid features of LIBs and faradic capacitor at low rate and a feature of faradic capacitor at high rate, and thus afforded enhanced reversible capacity and excellent cycling stability as well as a superior rate capability.

2 Experimental section

2.1 Synthesis of NGS

Dicyandiamide (DCDA, 99.5%), monohydrate glucose (MHG) and anhydrous ethanol (AHE) were used without further purification. In a typical synthesis, appropriate amounts of DCDA, MHG and AHE were poured into a milling pot, in which the mass ratio of DCDA to MHG was fixed to 10. The mixture was mixed for 4 h using a planet type ball mill, and then dried. Subsequently, the obtained powder of precursor was heated in two steps under a nitrogen atmosphere. In the low-temperature state, the precursor was heated to 580 ^oC by 2.2 ^oC min^{-1} and kept at this temperature for 4 h.[44,45] DCDA was pyrolyzed during this step to create layered stacks of GCN template, and the aromatic carbon intermediates resulted from MHG were enclosed within the interlayer gaps of GCN (denoted as GCN enclosed graphene, GEG). NGS was finally obtained after removing the GCN template from GEG by thermolysis at 800 ^oC for 2 h, MLG was contrastively prepared by heating the GEG at 1000 ^oC for 2 h. As a reference, graphene nanosheets (GNS) were also synthesized using the typical method of reducing exfoliated graphite oxides.[46]

2.2 Material characterization

Nanoscale Accepted Manuscript

Scanning electron microscopy (SEM) characterization was performed on a field emission JSM-6700F instrument, and transmission electron microscopy (TEM) image was captured on a JEOL-2010 instrument at an acceleration voltage of 200 KV. Elemental mapping images of NGS were scanned using energy filtered TEM (EFTEM, JEM-ARM200F). In order to reveal the changes that occurred during heat treatment at the high-temperature state, TG analysis for GEG, NGS and MLG were carried out with a Q5000 IR Thermogravimetric Analyzer (TGA, TA Instruments), in which the dried material was heated in nitrogen atmosphere by 10 ^{o}C min^{-1} from room temperature to 1000 ^{o}C. To evaluate the structural changes of GEG to NGS and MLG, X-ray diffraction (XRD) measurements were analyzed with Cu Kα radiation at λ = 1.054 Å on a Bruker AXS D8 X-ray diffractometer. The surface area and porosity were measured by the standard nitrogen adsorption isotherms at 77 K using an automated Micropore gas analyzer Autosorb-1 MP (Quantachrome Instruments) and data analysis was performed with Quantachrome software. Further, the crystallographic structure of the materials was determined using a Bruker AXS D8 X-ray diffractometer with Cu Kα radiation. X-ray photoelectron spectroscopy (XPS) (ESCALAB 250 Xi; Al anode X-ray source) was used to investigate the surface chemistries of the obtained material, and the Raman spectra was obtained with a high-resolution, dispersive Raman spectrometer system (Horiba-Jobin Yvon LabRam HR) equipped with a visible laser excitation of 514 nm.

2.3 Electrochemical test

Nanoscale Accepted Manuscript

The working electrodes were prepared by spreading a mixture of active mass (80 wt% for NGS, MLG and GNS electrodes, respectively and 60 wt% for GEG electrode), acetylene black (only added for GEG electrode, 20 wt%) and polyvinylidene fluoride (Kynar FLEX 910, Elf Atochem) binder dissolved in *N*-methylpyrrolidone (Fluka Inc., St. Louis, MO, USA) onto Cu foil (thickness 20 μm) current collector. The electrolyte consists of 1 M $LiPF_6$ in a mixture of isometric ethylene carbonate, dimethyl carbonate, and diethyl carbonate (Guotai-Huarong Co., Zhangjiagang, China). The electrochemical characterisations were conducted in 2025-type coin cells using Li foil (99.9%, China Energy Lithium Co., Ltd., Tianjin) as a counter electrode. Galvanostatically charge-discharge (GCD) experiments were conducted on a battery testing system (CT2001A, Land) over a range of 0.01~3 V vs. Li/Li^+. Cyclic voltammetry (CV) measurements were performed on an electrochemical workstation (Ivium Stat) within the range of 0~3 V. The reported specific capacities (SCs) are all normalized to the weight of active materials.

3 Results and discussion

To investigate the morphology and microstructure of the products, optical photographs, SEM and TEM images were taken from the as-prepared materials. As Figure 1 presents, different from the conventional brilliant yellow[45] of GCN (Figure 1a), GEG appeared as grayish-black bulk. The representative SEM image shows that the GEG consists of dense agglomerates with a size of several micrometers.After heating the GEG at 800 ^{o}C, “silk like” NGS was obtained without the presence of any residual GCN. According to the SEM and TEM images, the freestanding

Nanoscale Accepted Manuscript

graphene sheets display a layered morphology, intrinsic microscopic roughening and out-of-plane deformations for both NGS and MLG. Compare with the rich thick nanosheet of MLG, the NGS display a vague and very flexible appearance with a typical waving, indicating the sparing restacking of graphene layers in NGS. The microstructures of individual NGS were further examined by EFTEM and high-resolution TEM (HRTEM). As shown in Figure 2a-d, there is a uniform distribution of C, N and O elements throughout the graphene sheet. From these qualitative observations, the dense agglomerated GCN were significantly detracted, and thus the nitrogen dopant has evenly inserted into the graphene basal plane. The HRTEM image (Figure 2e) inspects the honeycomb-like molecular structure of the single nitrogen-doped graphene sheet, the more irregular domains verify the defects and/or functional groups in NGS basal plane.

The TG curve of GEG (Figure 3a) shows two weight loss (WL) steps. The first one is prior to 200 ^{o}C with a WL of 4.56% and could be attributed to the evaporation of the absorbed moisture.[47] The major part of the WL seems to occur at *ca*. 689 ^{o}C and the rapid WL of 90.53% was mainly caused by the pyrolysis of GCN template,[44,48] whereas the TG curves of both NGS and MLG (Figure 3b-c) show three WL steps. Prior to 100 ^{o}C, the rapid WL came from the desorption of free water in the graphene layers. The WL in the temperature range of 230~450 ^{o}C was predominantly caused by the elimination of organic residues in the samples. The major part of the WL occured above 600 ^{o}C, corresponding to the pyrolysis of functional groups and/or residual GCN. While the WL of 2.1% for MLG, the WL for

Nanoscale Accepted Manuscript

NGS is 22.1%, revealing that the nitrogen dopants decomposed almost completely at 1000 °C. According to the TG results, the mass ratios of the nitrogen components in NGS and MLG are ca. 23.6% and 2.1%, respectively. In addition, WL of absorbed free water below 100 °C for NGS (ca. 6.4%) is more obvious than that for MLG (ca. 1.3%), indicating the developed absorptive abilities as well as the enlarged surface area of the NGS.

The structure of the GCN can be considered as graphite-like single layers aligning each other along the hexagonal *c*-axis. As shown in Figure 4a, GEG has two diffraction peaks in consistence with the GCN.[49-51] The low-angle peak at 13.1° can be attributed to an in-plane structural packing motif, for example, the hole-to-hole distance of the nitride pores.[50] The strong and sharp peak at 27.4º can be indexed as (002) plane of the GCN, corresponding to the interlayer d-spacing of 0.325 nm.[45,49,51] Nevertheless, the peak around 27.4° in the XRD pattern of NGS was largely weakened and broadened, which can be attributed to the presence of intercalated "N defects" in the low-crystallized graphene plane.[48,52] Because the graphic structure of GCN was thoroughly wrecked after the pyrolysis at 800 °C, the much amplified peak around 13.1 ° should be attributed to the layered structure of NGS, corresponding to the interlamellar distance of 0.62 nm. It suggested that there could be some nitrogen groups propping out of the graphene plane besides the in-plane nitrogen dopants. These nitrogen groups could practically prevented the restacking of graphene layers and maintained the large interlayer distance, and thus increased the interfacial interaction of NGS and improved the diffusion of lithium

Nanoscale Accepted Manuscript

ion between graphene layers. The enhanced (002) peak of MLG, as well as (100) peak (around 42.5^{o}), verified a certain restacking of the un-propped graphene sheets after oversintering. In accordance with the above analyses, Raman analysis could also provide convincing evidences of the NGS and the restacked MLG. As shown in Figure 4b, the Raman spectra of the NGS and MLG exhibit two high intensity peaks around 1360 cm^{-1} (D band) and 1580 cm^{-1} (G band). The G band characteristic of the in-plane vibration from a layer of sp^2-hybridized carbon atoms provides the formation of graphitic carbon in both NGS and MLG, while the D band could be attributed to the defects or imperfections, reflecting the presence of disorder and the edges and boundaries of the graphene domains.[44,53] Crucially, however, the D/G intensity ratio (I_D/I_G=1.06) in NGS is slightly larger than that (I_D/I_G=1) in MLG, suggesting a relatively larger number of defects and disordered edge sites in NGS.[54] Furthermore, the enhanced 2D band around 2800 cm^{-1} in the Raman spectra of the NGS manifests less layers of graphene nanosheet in NGS.[53]

The specific surface area (SSA) and porous structure characteristics of NGS, MLG and GNS were investigated by nitrogen isothermal adsorption, as shown in Figure 5a. Compare with the type H2 IUPAC (International Union of Pure and Applied Chemistry) loop of the GNS, hysteresis loops of both NGS and MLG resemble type H3 classification, corresponding to the sheet particles or slit-shaped pores between parallel graphene sheets in NGS and MLG.[55] Somewhat differently, the hysteresis loop of NGS appeared at a lower relative pressure (RP) far from 0.4 (near 0.05), which is much lower than that of MLG (appeared at ca. 0.45 of RP),

Nanoscale Accepted Manuscript

indicating the presence of considerable amount of longer slit-shaped microporosity in NGS. The SSA and total pore volume (TPV) of NGS are 504 $m^2 g^{-1}$ and 0.96 $cm^3 g^{-1}$, respectively, being significantly higher than those of the GNS (483 $m^2 g^{-1}$ and 0.70 $cm^3 g^{-1}$) (Table 2). In contrast, the SSA and TPV of MLG are only 241 $m^2 g^{-1}$ and 0.55 $cm^3 g^{-1}$, respectively, revealed a very low micropore content, which can be attributed to the restacking of graphene layers after the elimination of nitrogen dopants when overcalcined at higher temperature. The corresponding porosity distribution in Figure 5b shows the dominant presence of microporosities and a few mesoporosities in both NGS and MLG. Prevailing porosities with a radius of ca. 0.36 nm might conform to the slit-shaped microporosities enclosed by in-plane monovacancies (and/or divacancies) and graphene layers[24], the mesoporosities with radius of ca. 1.7 nm could be analogous to the intergranular caves in graphene plane.[44] It is evident that the differential pore area [d$S(r)$] peak at radius of 0.36 nm in MLG largely decreased, showing the decline of in-plane monovacancies with the elimination of the nitrogen dopants.

As presented in Figure 6, signals of elements C, N, O are displayed in the wide XPS spectrum survey and the sharp C 1s peak manifestes the graphene lattices. As Table 1 shows, nitrogen atomic percentage in NGS is 19.46%, which is much higher than that in MLG and GNS, revealing the nitrogen dopants in NGS. The high-resolution spectra were taken on the C1s and N1s regions and could be deconvoluted into various components. Different from the sharp C1s peak (Figure 6d) of GNS, the broad NGS C1s spectra in Figure 6b can be resolved into four peaks

Nanoscale Accepted Manuscript

with binding energies of 284.9, 285.7, 286.2 and 288 eV, respectively. The primary peak at 284.9 eV is typically assigned to graphitic carbon in the literature,[30] but can also be attributed to sp2 C–N.[56] The peak at 288 eV is identified as sp^2-hybridized carbon in the aromatic ring attached to the nitrogen groups, the peaks at 285.7 and 286.2 eV corresponding to C–N and C–O/C=N, respectively.[30,33,57] However, the peak at 286.2 eV disappeared in MLG C1s spectra (Figure 6c), and a new peak at 290.3 eV emerged, indicating the transformation of hydroxyls to carboxylate carbon (O–C=O).[58] The N1s spectra of NGS (Figure 6e) reveales three major components corresponding to pyridinic nitrogen (398.46 eV), pyrrolic nitrogen (400.17 eV) and graphitic nitrogen (N-(C)3, 401.2 eV), respectively.[33,47,56,59-61] According to the report by Thomas A et al,[60] GCN could transform into cyano fragments and nitrogen when was heated to 700 ^{o}C. It is speculated that nitrogen might be introduced into the graphene lattice by the electrophilic substitution reaction between cyano fragments and actived carbon atoms in graphene. Signals of pyrrolic nitrogen in the N1s spectra of MLG could not be detected, and the peaks of pyridinic nitrogen and graphitic nitrogen were significantly weakened, displaying the elimination of nitrogen dopants in MLG after postannealing.

The electrochemical performances of the as-prepared materials were firstly evaluated by using galvanostatic charge/discharge measurements at a current density of 100 mA g^{-1} over the voltage range 0.05~3.0 V vs. Li/Li^+. Figure 7(a-d) shows the 1^{st}, 2^{nd}, 50^{th} and 100^{th} charge/discharge curves and cyclic performances of the NGS, MLG, GEG and GNS electrodes. The first cycle discharge/charge SCs of the NGS, MLG,

Nanoscale Accepted Manuscript

GEG and GNS electrodes are 1859.6/832.4, 840.5/269.1, 621.5/128.5, and 1260.1/571.4 mAh g^{-1}, respectively. The first coulombic efficiency (CE) of the NGS electrode is 44.8%, which is roughly equal to GNS (45.3%), and much higher than MLG (32.0%) and GEG (20.7%). Nevertheless, the first CE of NGS is lower than the commercial graphite, it could be attributed mainly to the formation of solid electrolyte interphase (SEI) film on graphene sheets[46] and the irreversible reactions of lithium ion with the in-plane graphitic nitrogen sites or other undesirable dopants,[36] and some strategies could be taken to boost the first efficiency.[36,37,62,63] Similar to the typical nanosized carbonaceous materials,[5,16,46] the slopes of the first discharge curves started from 3.0 V, without distinct potential plateaus. During the charge process, for MLG and GNS, the slopes started approximately 1.2 V (vs. Li/Li^+) and have large SCs below 1.0 V with a distinguishable plateau, corresponding to the Li^+ deintercalation from graphene layers.[5,64,65] Whereas, the charge profiles of NGS displayed appreciable voltage hysteresis, indicating the extraction of Li^+ from the slit-shaped microporosity has to go through the "way" of graphene crystallites, in which the inserted lithium ions were removed from entire voltage range, and without distinct potential plateaus in charge curves. Details of the first charge/discharge processes for NGS and MLG electrodes could be reflected as peaks in the differential capacity versus voltage plots, several reduction and oxidation peaks are clearly observed for NGS and MLG (Figure 7e), respectively. According to the reaction mechanism proposed in the earlier studies,[4,46] the peaks at 0.5~1.0 V in discharge process are mainly caused by the SEI formation, i.e., the

Nanoscale Accepted Manuscript

reaction of lithium ions with the active sites and decomposition of electrolytes on the surface of graphene electrodes, which are the main reasons of the initial irreversible capacity. These peaks can be typically enhanced by increasing the SSA and structural disorder of the electrode materials, and thus, enhanced peak of NGS can be attributed to the larger surface-to-volume ratio and surface electrochemical reactivity. In addition, comparing with that of the MLG, an extra discharge peak appeared around 1.56 V for NGS electrode, which practically disappeared after the first cycle, might probably associate with the consumption of lithium ions in the irreversible reaction with the graphitic nitrogen and/or other impurities.[26-36]

For the subsequent cycles, it is generally believed that the discharge capacity below 0.5 V (vs. Li/Li^+) assigns to lithium insertion into the graphene layers (lithium insertion capacity, LIC), yet the capacity above 0.5 V (vs. Li/Li^+) could be associated with the faradic capacitance resulting from the adsorption of Li^+ on pyridinic or pyrrolic defect structures.[5,15,26,65,66] As shown in Table 3, the LIC of NGS (377.7 mAh g^{-1}) were marginally higher than that of the GNS electrode (359.8 mAh g^{-1}). Despite the close SSA, however, comparing with that of the GNS electrode, the NGS electrode delivered a much higher faradic capacity (FC) of 349.4 mAh g^{-1}, about 3 times that of the GNS electrode (118 mAh g^{-1}), and it is also the main contribution to the high total capacity (TC) of NGS, manifesting the outstanding interfacial properties of the NGS. Figure 7f shows the cycling performance of the NGS, MLG, GEG and GNS electrode at a current density of 100 mA g^{-1} for 108 cycles. It is worth noting that the NGS electrode presented a much improved discharge capacity,

Nanoscale Accepted Manuscript

which was gradually increased after 30 cycles, and 770.8 mAh g^{-1} was achieved after 108 cycles, nearly two times than that of the MLG (441 mAh g^{-1}) or GNS (460.5 mAh g^{-1}), suggesting excellent cycling performance of NGS electrode.[31] It is speculated that the curious phenomenon of gradually increased capacity might owe to the conversion of graphitic nitrogen into pyridinic structure and/or the proliferation of in-plane defects during the electrochemical cycling.

To further investigate the electrochemical performance of the NGS, rate capabilities and high rate cycling performances of the NGS electrode were examined (Figure 8). An excellent high rate capability was determined for NGS, charge capacity of 666 mAh g^{-1} was obtained after the first 80 cycles at a low current density of 100 mA g^{-1}, and then it slowly reduced to 441.2, 380.5, and 275.2 mAh g^{-1} at current density of 500, 1000, and 2500 mA g^{-1}, respectively. Superior capacity of 771.3 mAh g^{-1} could be resumed in 121st cycle when the current density reduced back to 100 mA g^{-1}. And, as note while the electrode was cycled at 2500 mA g^{-1} again, the reversible capacity could recover to 339.2 mAh g^{-1}, afterwards, increase to 486.3 mAh g^{-1} after 344 cycles. Moreover, the ability of the NGS electrode retained the storage capacity at very high rates, as well as a fascinating high rate cyclic performance, what should be noted. Over 43% of the storage capacity was retained for a 100-fold increase in rate, i.e., it was achieved a reversible capacity of 333 mAh g^{-1} (595^{th} cycle) at a current density as high as 10000 mA g^{-1} (corresponding to a discharge or charge time of ca. 120 s), significantly higher than those of the graphene-based electrodes reported previously. Furthermore, this capacity is retained

Nanoscale Accepted Manuscript

at 280.6 mAh g^{-1} even after 1200 cycles, attaining capacity retention of 84.3% at the current density of 10000 mA g^{-1} from 595th to 1200th cycle. To the best of our knowledge, such an excellent high-rate performance is superior to all existing graphene-based materials reported for LIBs.[6,25,30,31,34,39,42,65,67-70] The discharge FC, LIC and TC of the NGS at various current densities are shown in Table 4. When cycled at low rate, the LIC and TC are roughly equivalent. With increasing current density, the LIC decreased significantly as it was previsedly, yet the FC tardily decreased, and FC/TC increased gradually, when cycled at the high current density of 10000 mA g^{-1}, FC contributed most of TC (70.28%), corresponding to the rapid lithium adsorption in NGS.

CV profiles (Figure 9) at different scan rates were processed to survey the electrochemical cycling behaviors of the NGS and MLG electrodes. CV curves of MLG electrode exhibit a pair of peaks locating below 0.5 V, corresponding to the intercalation and deintercalation process of lithium ions deservedly. Nevertheless, distinct from that of the MLG, sweeping at 1 mV s^{-1}, the CV curve of NGS electrode appeared a typical capacitive behavior among the potential range of 0.5~3 V, corresponding to the Li^+ adsorption in trimerized pyridine-type nitrogen sites, and a higher cathodic current peak at near 0 V which is related to Li^+ intercalation in graphitic structure.[24,26,35-37,71] When the scan rate was increased, it is intriguing to see that the shape of the CV curve, over the entire potential range, was transformed into a quasi-rectangular gradually, and correspondingly, the lithium intercalation peak was substantially decreased, indicating that the reactions of Li^+ with pyridinic

Nanoscale Accepted Manuscript

structure were the predominant process for the high-capacity of NGS at high rate cycling, and the lithium storage behavior in NGS were more like an ideal supercapacitor.

To understand the excellent electrochemical performance, a schematic illustration (Figure 10) for lithium-storage mechanism of NGS was proposed. NGS was finally obtained after removing the GCN template from GEG, and it is considered that nitrogen atoms were doped into the graphene lattice dominantly in the form of pyridinic structure. The pyridinic dopant could enlarge the binding energies of the lithium atom with graphene planes and simultaneously lower the energy barrier of Li^+ diffusion. Thus more Li^+ could be embedded on the NGS plane and consequently exhibited an increased storage capacity.[26,35,37] Furthermore, defects including the intergranular caves and the in-plane vacancies offer the large electrolyte contact area and also empower the lithium penetrating cross the gaphene layers,[24] which enable a significant reduction of the Li^+ diffusion path and thus can expedite the ion transport, exhibiting a superior rate capabilities and high rate cycling performances.

4 Conclusions

A facile bottom-up strategy was developed to fabricate NGS from glucose by using a sacrificial template synthesis method. It was found that three main types of nitrogen dopants (pyridinic nitrogen, pyrrolic nitrogen and graphitic nitrogen) were introduced into the graphene lattice, and inimitable microporous structure of NGS with a high SSA of 504 m^2 g^{-1} was obtained. Particularly, with a hybrid feature of lithium ion batteries and faradic capacitor at a low rate and a faradic capacitor

Nanoscale Accepted Manuscript

feature at a high rate, the NGS presented a superior lithium storage performance. During electrochemical cycling, the NGS electrode afforded enhanced reversible capacity of 832.4 mAh g^{-1} at 100 mA g^{-1} and excellent cycling stability of 750.7 mAh g^{-1} after 108 cycles. Furthermore, astonishing rate capability of 333 mAh g^{-1} at 10000 mA g^{-1} and high rate cycle performance of 280.6 mAh g^{-1} even after 1200 cycles were also achieved, highlighting the significance of nitrogen doping on the maximum utilization of graphene-based materials for advanced lithium storage. More importantly, the developed bottom-up synthetic strategy and the obtained unique nanoarchitectures are envisaged to pave the way toward a design and fabrication of novel graphene-based composites with enhanced properties for high energy and high power lithium storage and/or other applications.

Acknowledgments

The authors acknowledge financial supports from the Fund from National Natural Science Foundation of China for Innovative Research Group (Grant 51221462), the Jiangsu Ordinary University Graduate Innovative Research Programs (CXZZ12_0943, CXZZ13_0952), Jiangsu Planned Projects for Postdoctoral Research Funds (1201030C), and the Priority Academic Program Development of Jiangsu Higher Education Institutions.

References and Notes

1. Zhao, X.; Hayner, C. M.; Kung M. C.; Kung, H. H. *Adv. Energy Mater.* **2011**, *1*, 1079–1084.

2. Novoselov, K. S.; Geim, A. K.; Morozov, S. V.; Jiang, D.; Zhang, Y.; Dubonos,

Nanoscale Accepted Manuscript

S. V.; Grigorieva, I. V.; Firsov. A. A. *Science* **2004**, *306*, 666–669.

3. Sattayasamitsathit, S.; Gu, Y.; Kaufmann, K.; Jia, W.; Xiao, X.; Rodriguez, M.; Minteer, S.; Cha, J.; Burckel, D. B.; Wang, C.; Polsky, R.; Wan, J. *J. Mater. Chem. A* **2013**, *1*, 1639–1645.
4. Wang, G. X.; Shen, X. P.; Yao, J.; Park, J. *Carbon* **2009**, *47*, 2049–2053.
5. Yoo, E. J.; Kim, J.; Hosono, E.; Zhou, H. S.; Kudo, T.; Honma, I. *Nano Lett.* **2008**, *8*, 2277–2282.
6. Zhao, X.; Hayner, C. M.; Kung, M. C.; Kung, H. H. *ACS Nano* **2011**, *5*, 8739–8749.
7. Wu, Z. S.; Zhou, G. M.; Yin, L. C.; Ren, W.; Li, F.; Cheng, H. M. *Nano Energy* **2012**, *1*, 107–131.
8. Tian, L. L.; Zhuang, Q. C.; Li, J.; Wu, C.; Shi, Y. L.; Sun, S. G. *Electrochim. Acta* **2012**, *65*, 153–158.
9. Yang, S.; Feng, X.; Ivanovici, S.; Müllen, K. *Angew. Chem. Int. Ed.* **2010**, *49*, 8408–8411.
10. Paek, S.M.; Yoo, E.; Honma, I. *Nano Lett.* **2009**, *29*, 72–75.
11. Wang, H. L.; Cui, L. F.; Yang, Y.; Casalongue, H. S.; Robinson, J. T.; Liang, Y. Y.; Cui, Y.; Dai, H. J. *J. Am. Chem. Soc.* **2010**, *132*, 13978–13980.
12. Tian, L. L.; Wei, X. Y.; Zhuang, Q. C.; Wu, C.; Xie, R. L.; Zong, Z. M.; Cui, Y. L.; Sun. S. G. *Nano*, **2013**, *8*, 1350068.
13. Tian, L. L.; Wei, X. Y.; Zhuang, Q. C.; Zong, Z. M.; Sun. S. G. *Acta Chim. Sinica*, **2013**, *71*, 1270–1274.

Nanoscale Accepted Manuscript

14. Yang, S.; Gong, Y.; Liu, Z.; Liang, Z.; Hashim, D. P.; Ma, L.; Vajtai, R.; Ajayan, P. M. *Nano Lett.* **2013**, *13*, 1596–1601.

15. Wang,G. X.; Shen, X. P.; Yao, J.; Park, J. *Carbon* **2009**, *47*, 2049–2053.

16. Pan, D.Y.; Wang, S.; Zhao, B.; Wu, M. H.; Zhang, H. J.; Wang, Y.; Jiao, Z. *Chem. Mater.* **2009**, *21*, 3136–3142.

17. Pollak, E.; Geng, B. S.; Jeon, K. J.; Lucas, I. T.; Richardson, T. J.; Wang, F.; Kostecki,. R. *Nano Lett.* **2010**, *10*, 3386–3388.

18. Uthaisar, C.; Barone, V. *Nano Lett.* **2010**, *10*, 2838–2842.

19. Lee, E.; Persson, K. A. *Nano Lett.* **2012**, *12*, 4624−4628.

20. Kaskhedikar, N. A.; Maier, J. *Adv. Mater.* **2009**, *21*, 2664–2680.

21. Liang, M. H.; Zhi, L. J. *J. Mater. Chem.* **2009**, *19*, 5871–5878.

22. Ferre-Vilaplana, A. *J. Phys. Chem. C* **2008**, *112*, 3998–4004.

23. Ataca, C.; Akturk, E.; Ciraci, S.; Ustunel, H. *Appl. Phys. Lett.* **2008**, *93*, 043123.

24. Yao, F.; Günes, F.; Ta, H. Q.; Lee, S. M.; Chae, S. J.; Sheem, K. Y.; Cojocaru, C. S.; Xie, S. S.; Lee, Y. H. *J. Am. Chem. Soc.* **2012**, *134*, 8646−8654.

25. Wu, Z. S.; Ren, W.; Xu, L.; Li F.; Cheng, H. M. *ACS Nano* **2011**, *5*, 5463–5471.

26. Ma, C.; Shao, X.; Cao, D. *J. Mater. Chem.* **2012**, *22*, 8911–8915.

27. Mao, Y.; Duan, H.; Xu, B.; Zhang, L.; Hu, Y.; Zhao, C.; Wang, Z.; Chen, L.; Yang, Y. *Energy Environ. Sci.* **2012**, *5*, 7950–7955.

28. Panchakarla, L. S.; Subrahmanyam, K. S.; Saha, S. K.; Govindaraj, A.; Krishnamurthy, H. R.; Waghmare, U. V.; Rao, C. N. R. *Adv. Mater.* **2009**, *21*, 4726–4730.

Nanoscale Accepted Manuscript

29. Jin, Z.; Yao, J.; Kittrell, C.; Tour, J. M. *ACS Nano* **2011**, *5*, 4112–4117.

30. Reddy, A. L.; Srivastava, A.; Gowda, S. R.; Gullapalli, H.; Dubey, M.; Ajayan, P. M. *ACS Nano* **2010**, *4*, 6337–6342.

31. Li, X.; Geng, D.; Zhang, Y.; Meng, X.; Li, R.; Sun, X. *Electrochem. Commun.* **2011**, *13*, 822–825.

32. Geng, D.; Yang, S.; Zhang, Y.; Yang, J.; Liu, J.; Li, R.; Sham, T. K.; Sun, X.; Ye S.; Knights, S. *Appl. Surf. Sci.* **2011**, *257*, 9193–9198.

33. Wang, H. B.; Zhang, C. J.; Liu, Z. H.; Wang, L.; Han, P.; Xu, H.; Zhang, K.; Dong, S.; Yao, J.; Cui, G. *J. Mater. Chem.* **2011**, *21*, 5430–5434.

34. Deng, D. H.; Pan, X. L.; Yu, L.; Cui, Y.; Jiang, Y. P.; Qi, J.; Li, W. X.; Fu, Q.; Ma, X. C.; Xue, Q. K.; Sun, G. Q.; Bao, X. H. *Chem. Mater.* **2011**, *23*, 1188–1193.

35. Kong, K. X.; Chen, W. Q. *Phys. Chem. Chem. Phys.* **2013**, *15*, 12982–12987.

36. Veith, G. M.; Baggetto, L.; Adamczyk, L. A.; Guo, B.; Brown, S. S.; Sun, X. G.; Albert, A. A.; Humble, J. R.; Barnes, C. E.; Bojdys, M. J.; Dai, S.; Dudney, N. J. *Chem. Mater.* **2013**, *25*, 503−508.

37. Yu, Y. X. *Phys. Chem. Chem. Phys.* **2013**, *15*, 16819−16827.

38. Wang, H.; Xie, M.; Thia, L.; Fisher, A.; Wang, X. *J. Phys. Chem. Lett.* **2014**, *5*, 119−125.

39. Hu, T.; Sun, X.; Sun, H.; Xin, G.; Shao, D.; Liu, C.; Lin, J. *Phys. Chem. Chem. Phys.* **2014**, *16*, 1060−1066.

40. Shao, Y.; Zhang, S.; Engelhard, M. H.; Li, G.; Shao, G.; Wang, Y.; Liu, J.; Aksay,

Nanoscale Accepted Manuscript

I. A.; Lin, Y. *J. Mater. Chem.* **2010**, *20*, 7491–7496.

41. Ding, D.; Song, Z. L.; Cheng, Z. Q.; Liu W. N.; Nie, X. K.; Bian, X.; Chen, Z.; Tan, W. *J. Mater. Chem. A* **2014**, *2*, 472–477.
42. Zhou, X.; Bao, J.; Dai, Z.; Guo, Y. G. *J. Phys. Chem. C* **2013**, *117*, 25367−25373.
43. Long D.; Li, W.; Ling, L.; Jin, M.; Mochida, I.; Yoon S. H. *Langmuir* **2010**, *26*, 16096–16102.
44. Li, X. H.; Kurasch, S.; Kaiser, U.; Antonietti, M. *Angew. Chem. Int. Ed.* **2012**, *51*, 9689–9692.
45. Wang, X.; Maeda, K.; Thomas, A.; Takanabe, K.; Xin, G.; Carlsson, J. M.; Domen, K.; Antonietti, M. *Nat. Mater.* **2008**, *8*, 76–80.
46. Tian, L. L.; Zhuang, Q. C.; Li, J.; Shi, Y. L.; Chen, J. P.; Lu, F.; Sun, S. G. *Chinese Sci. Bull.* **2011**, *56*, 3204–3212.
47. Bian, S. W.; Ma, Z.; Song, W. G. *J. Phys. Chem. C* **2009**, *113*, 8668–8672.
48. Parvez, K.; Yang, S.; Hernandez, Y.; Winter, A.; Turchanin, A.; Feng, X.; Müllen, K. *ACS Nano*, **2012**, *11*, 9541–9550.
49. Niu, P.; Zhang, L.; Liu, G.; Cheng, H. M. *Adv. Funct. Mater.* **2012**, *22*, 4763–4770.
50. Goettmann, F.; Fischer, A.; Antonietti, M.; Thomas, A. *Angew. Chem. Int. Ed.* **2006**, *45*, 4467–4471.
51. Yan, H.; Chen, Y.; Xu, S. *Int. J. Hydrogen Energ.* **2012**, *37*, 125–133.
52. Qu, L.; Liu, Y.; Baek, J. B.; Dai, L. *ACS Nano*, **2010**, *4*, 1321–1326.

Nanoscale Accepted Manuscript

53. Sun, J.; Liu, H.; Chen, X.; Evans, D. G.; Yang, W.; Duan, X. *Chem. Commun.* **2012**, *48*, 8126–8128.

54. Luo, Z.; Lim, S.; Tian, Z.; Shang, J.; Lai, L.; MacDonald, B.; Fu, C.; Shen, Z.; Yu, T.; Lin, J. *J. Mater. Chem.* **2011**, *21*, 8038–8044.

55. Lian, P.; Zhu, X.; Liang, S.; Li, Z.; Yang, W.; Wang, H. *Electrochim. Acta* **2010**, *55*, 3909–3914.

56. Huang, J.; Liu, P.; Antonietti, M.; Wang, X. *J. Mater. Chem.* **2011**, *21*, 13032–13039.

57. Liu, Y. C.; Lu, D. N. *Plasma Chem. Plasma Process*. **2006**, *26*, 119–126.

58. Yuan, C.; Chen, W.; Yan, L. *J. Mater. Chem.* **2012**, *22*, 7456–7460.

59. Song, J.; Xu, T.; Gordin, M. L.; Zhu, P.; Lv, D.; Jiang, Y. B.; Chen, Y.; Duan, Y.; Wang, D. *Adv. Funct. Mater.* **2014**, *24*, 1243–1250.

60. Thomas, A.; Fischer, A.; Goettmann, F.; Antonietti, M.; Müller, J. O.; Schlögl, R.; Carlsson, J. M. *J. Mater. Chem.* **2008**, *18*, 4893–4908.

61. Dong, F.; Wu, L.; Sun, Y.; Fu, M.; Wu, Z.; Lee, S. C. *J. Mater. Chem.* **2011**, *21*, 15171–15174.

62. Aurbach, D.; Gamolsky, K.; Markovsky, B.; Gofer, Y.; Schmidt, M.; Heider, U. *Electrochim. Acta* **2002**, *47*, 1423–1439.

63. Wu, Z. S.; Xue, L.; Ren, W.; Li, F.; Wen, L.; Cheng, H. M. *Adv. Funct. Mater.* **2012**, *22*, 3290–3297.

64. Guo, P.; Song, H.; Chen, X. *Electrochem. Commun.* **2009**, *11*, 1320–1324.

65. Jiang, Z.; Pei, B.; Manthiram, A. *J. Mater. Chem. A* **2013**, *1*, 7775–7781.

Nanoscale Accepted Manuscript

66. Yazami, R.; Deschamps, M. *J. Power Sources* **1995**, *54*, 411–415.

67. Brownson, D. A. C.; Kampouris, D. K.; Banks, C. E. *J. Power Sources* **2011**, *196*, 4873–4885.

68. Han, S.; Wu, D.; Li, S.; Zhang, F.; Feng, X. *Small* **2013**, *9*, 1173–1187.

69. Fang, Y.; Lv, Y.; Che, R.; Wu, H.; Zhang, X.; Gu, D.; Zheng, G.; Zhao, D. *J. Am. Chem. Soc.* **2013**, *135*, 1524−1530.

70. Mukherjee, R.; Thomas, A. V.; Krishnamurthy, A.; Koratkar, N. *ACS Nano* **2012**, *6*, 7867–7878.

71. Paek, E.; Pak, A. J.; Kweon, K. E.; Hwang, G. S. *J. Phys. Chem. C* **2013**, *117*, 5610−5616.

Nanoscale Accepted Manuscript

Tables

Table 1. Surface atomic percentages of C, N and O in NGS, MLG and GNS determined by XPS.

Table 2. BET surface areas and cumulative pore volume of NGS, MLG and GNS obtained from nitrogen adsorption isotherms at 77 K.

Table 3. FC, LIC and TC of the 100th cycle discharge process for NGS, MLG, GEG and GNS electrodes at 100 mA g^{-1}.

Table 4. FC, LIC and TC of the NGS electrode at different current densities.

Table 1

Sample	C1s	N1s	O1s
NGS	74.74	19.46	5.80
MLG	90.05	6.20	3.75
GNS	93.52	2.04	4.44

Table 2

Sample	SSA (m^2 g^{-1})	TPV (cm^3 g^{-1})
NGS	504	0.96
MLG	241	0.55
GNS	483	0.70

Table 3

Sample	Capacity (mAh g^{-1})			FC/TC (%)
	FC	LIC	TC	
NGS	349.4	377.7	727.1	48.05
MLG	182.8	252.2	435	42.02
GEG	45	52.6	97.6	46.11
GNS	118	359.8	477.8	24.70

Table 4

Current density	Capacity (mAh g^{-1})			FC/TC (%)	Cycle number
(mA g^{-1})	FC	LIC	TC		
100	330.6	348.6	679.2	48.67	80
500	233.9	201.9	435.8	53.67	92
1000	211.1	170.5	381.6	55.32	102
2500	276.5	212.4	488.9	56.56	344
5000	247.2	162.5	409.7	60.34	594
10000	197.2	83.4	280.6	70.28	1200

Nanoscale Accepted Manuscript

Figure captions

Figure 1. (a) Optical image of GCN, (b) SEM image of GEG (the insert is the optical image), Representative SEM and TEM images of (c and e) NGS and (d and f) MLG.

Figure 2. EFTEM elemental mapping and HRTEM images of a single NGS. (a) Zero-loss image, (b) C-K mapping, (c) N-K mapping, (d) O-K mapping, (e) HRTEM, (g) Schematic representation of nitrogen-doped graphene.

Figure 3. TG results of (a) GEG, (b) MLG and (c) NGS. DW denotes differential weight.

Figure 4. (a) XRD patterns of GEG, MLG and NGS, and (b) Raman spectra of NGS and MLG.

Figure 5. (a) Nitrogen adsorption-desorption isotherms and (b) the corresponding porosity distribution of NGS, MLG and GNS. VA and HPW denote volume adsorbed and half pore width, respectively.

Figure 6. XPS survey spectra of graphenes synthesized by sacrificial template strategy and reducing exfoliated graphite oxides method. (a) Wide XPS spectra of NGS, MLG, and GNS, (b) high-resolution XPS C1s spectra and their fitting results of NGS, (c) MLG and (d) GNS; (e) high-resolution XPS N1s spectra and their fitting results of NGS and (f) MLG. BE denotes binding energy.

Figure 7. Electrochemical characterizations of a half-cell composed of graphene electrode and Li over the voltage range 0.05~3.0 V vs. Li/Li^+ at a current density of 100 mA g^{-1}. Charge–discharge profiles for 1st, 2nd, 50th, and 100th cycle for (a) NGS, (b) MLG, (c) GEG and (d) GNS; (e) Initial 2 cycles charge-discharge differential

Nanoscale Accepted Manuscript

capacity versus voltage plots (dQ/dV) of NGS and MLG and (f) Cyclic performances and CE.

Figure 8. Rate capabilities and high rate cycling performances of NGS electrode at various current densities over the voltage range 0.05~3.0 V vs. Li/Li^+. (A) Charge-discharge profiles, (B) High rate cycling performances. (a) 100 mA g^{-1}, (b) 500 mA g^{-1}, (c) 1000 mA g^{-1}, (d) 2500 mA g^{-1}, (e) 5000 mA g^{-1}, (f) 10000 mA g^{-1}.

Figure 9. CV curves of the (a) MLG and (b) NGS electrodes in the voltage range of 0~3 V at 1, 5 and 10 mV s^{-1} vs. Li/Li^+.

Figure 10. Schematic illustration for the lithium-storage mechanism of NGS.

Nanoscale Accepted Manuscript

Figure 1

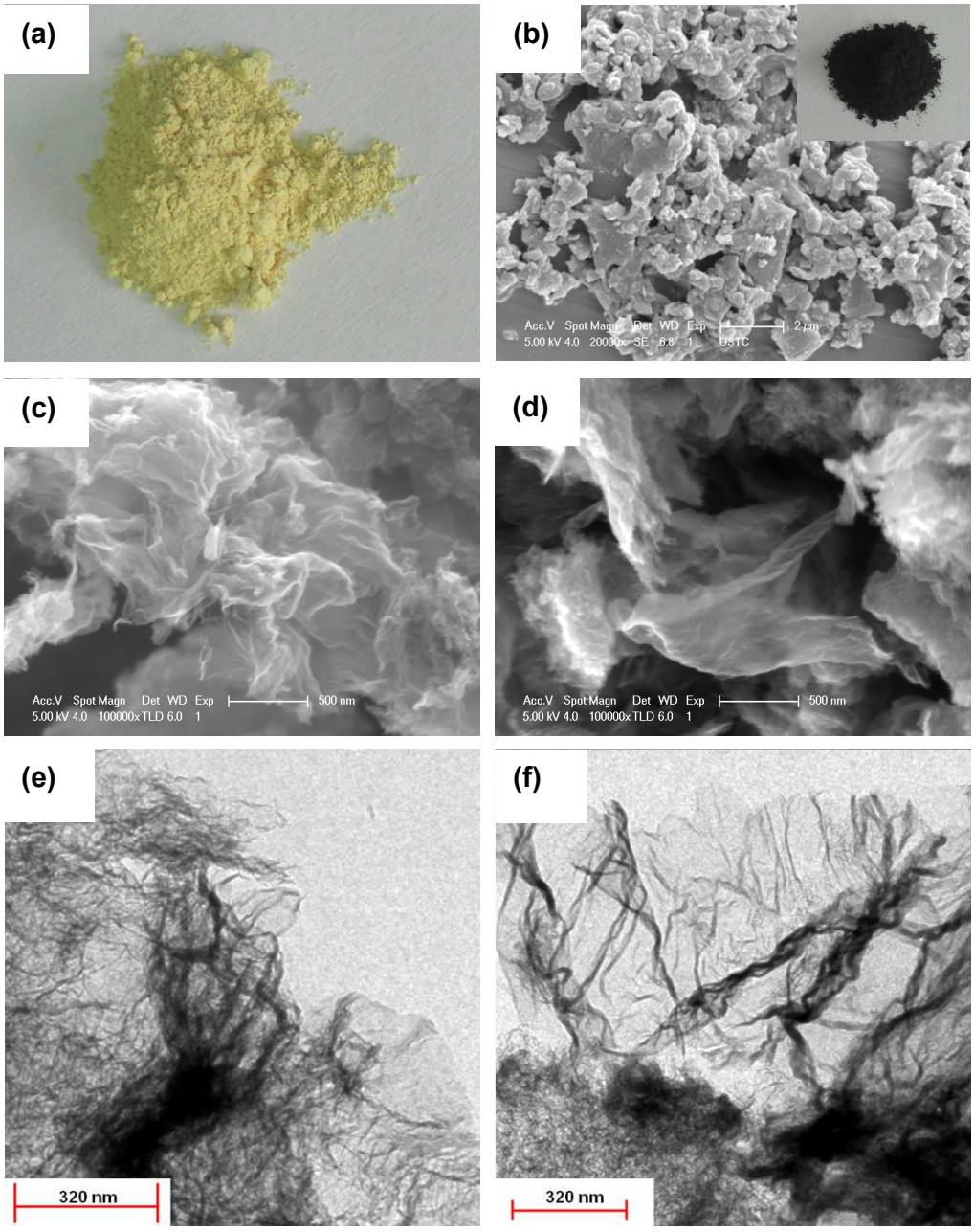

Nanoscale Accepted Manuscript

Figure 2

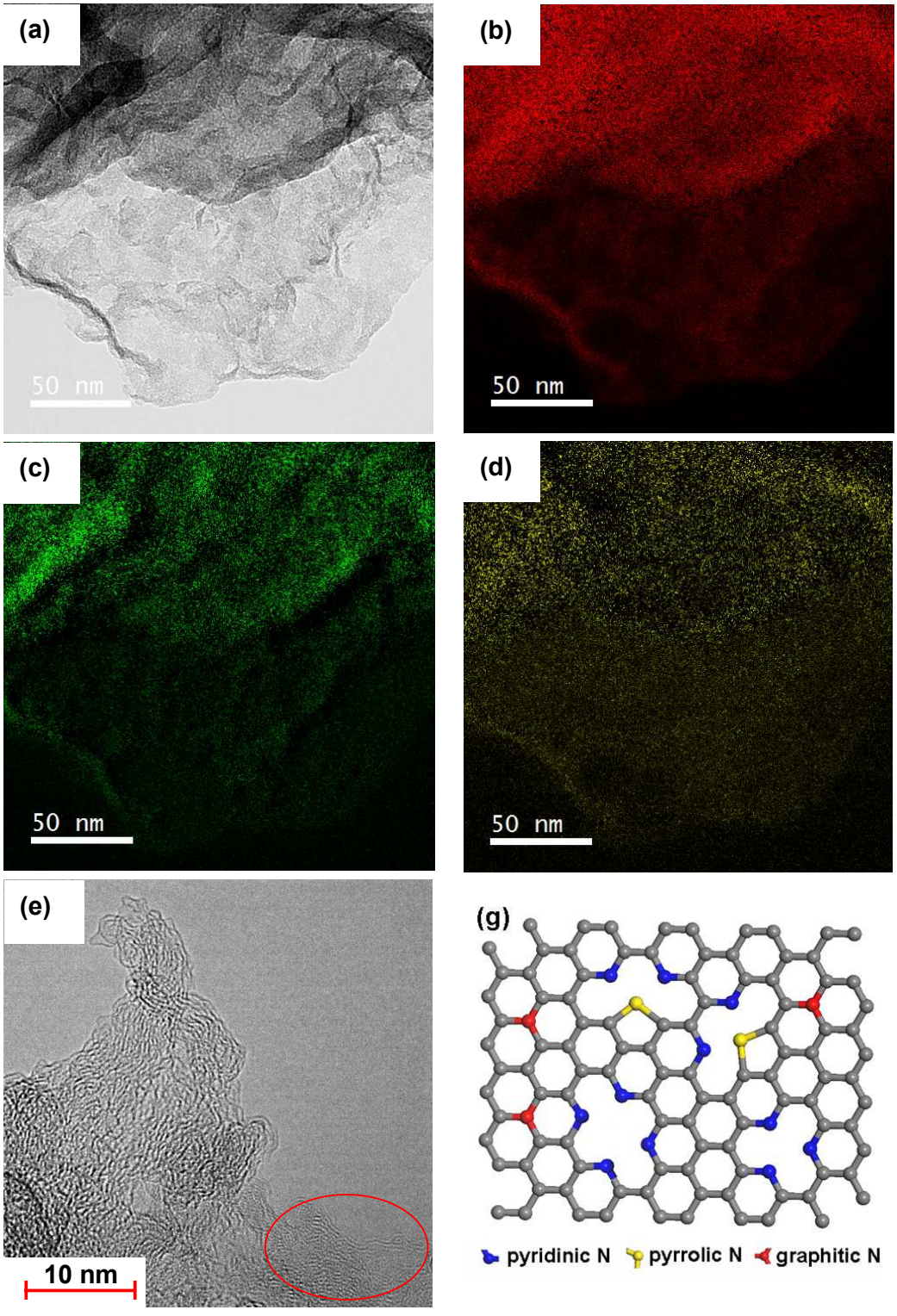

Nanoscale Accepted Manuscript

Figure 3

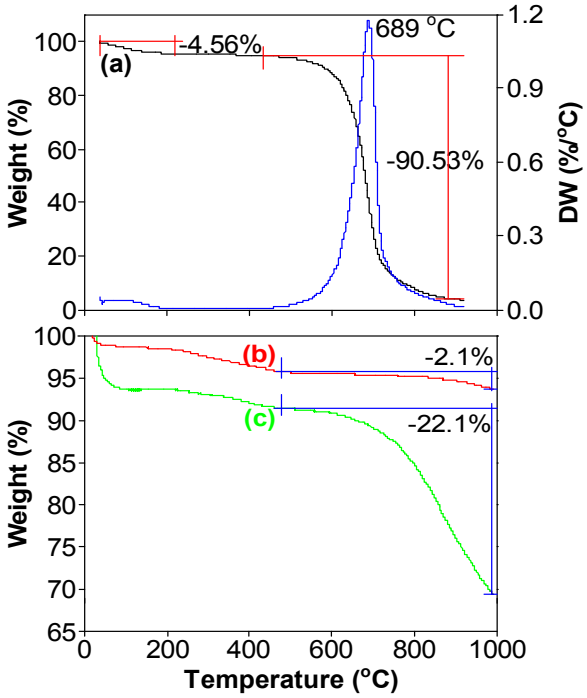

Figure 4

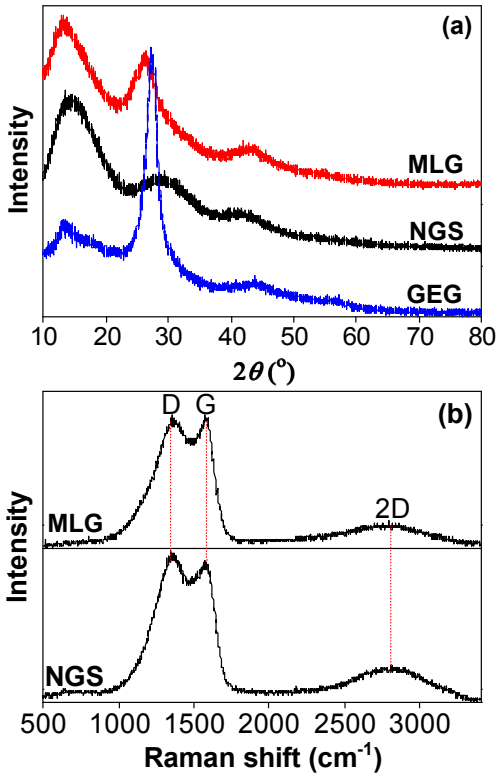

Nanoscale Accepted Manuscript

Figure 5

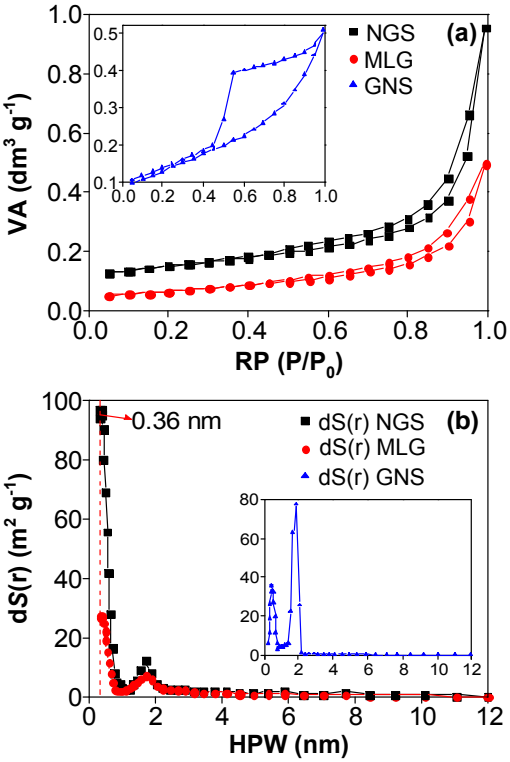

Nanoscale Accepted Manuscript

Figure 6

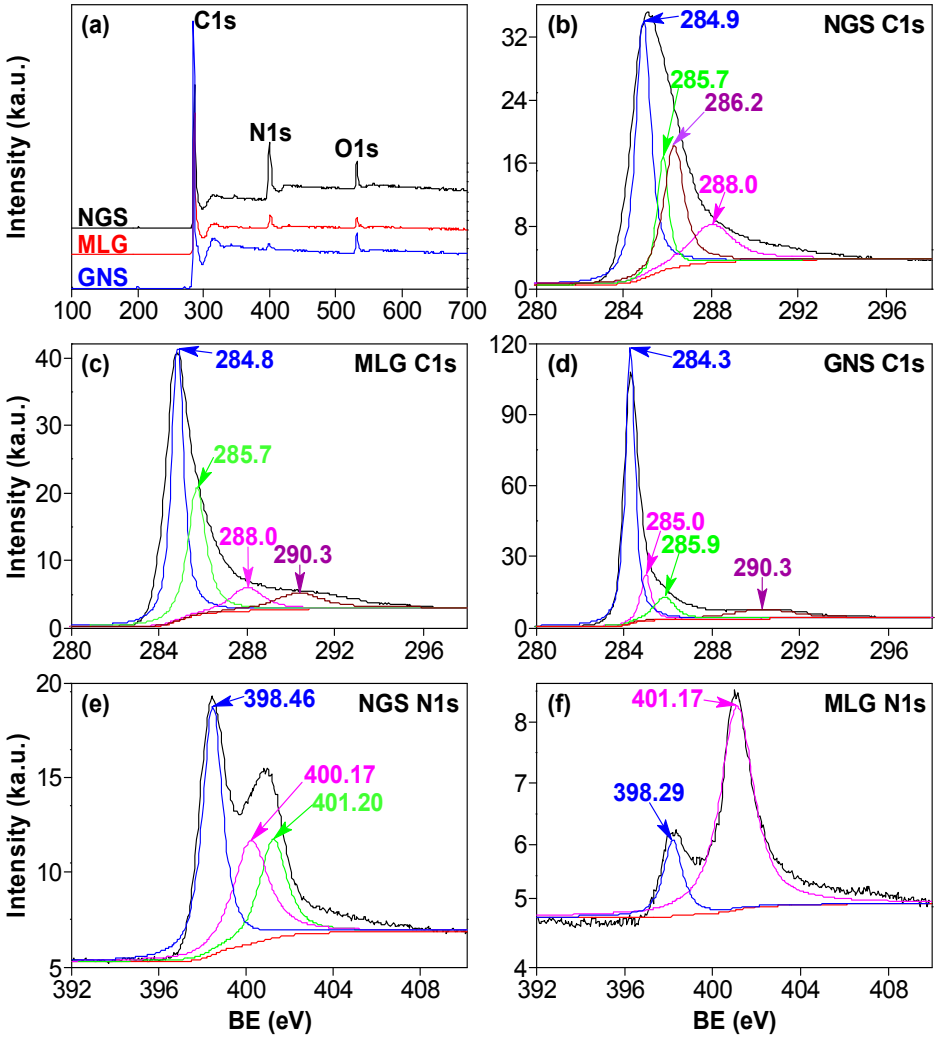

Nanoscale Accepted Manuscript

Figure 7

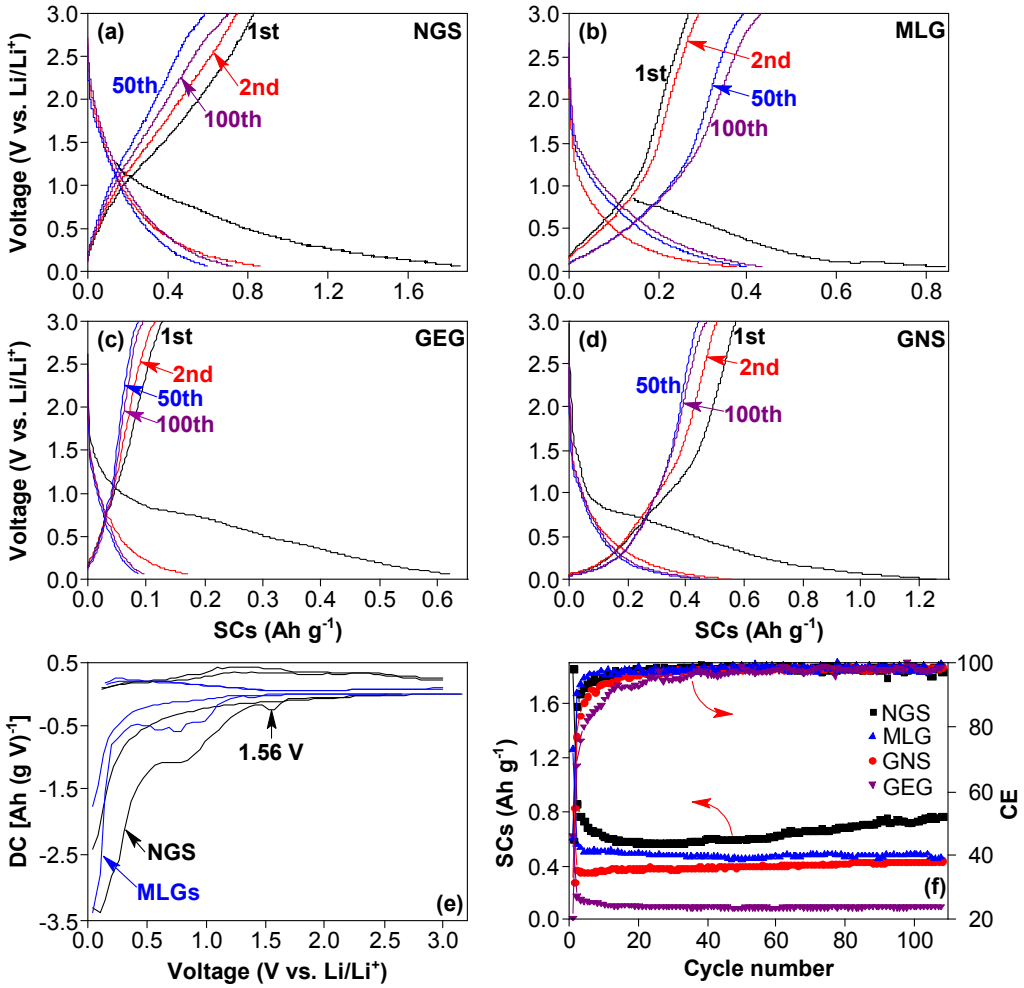

Nanoscale Accepted Manuscript

Figure 8

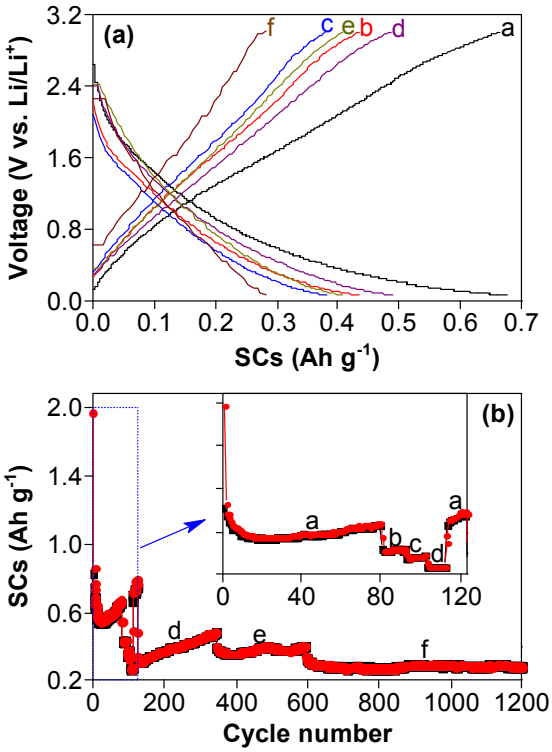

Figure 9

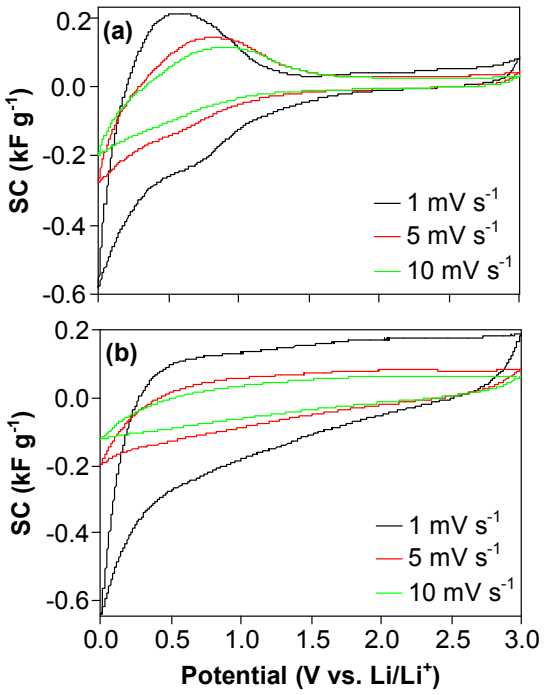

Nanoscale Accepted Manuscript

Figure 10

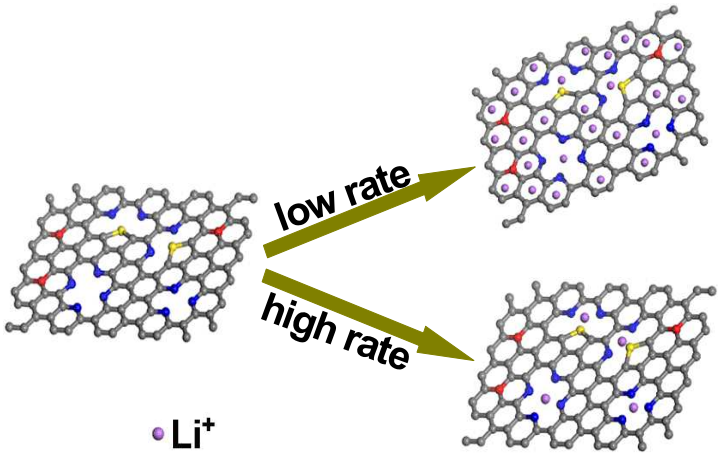

Nanoscale Accepted Manuscript